

# Radon-based Image Reconstruction for MPI using a continuously rotating FFL

Stephanie Blanke\* and Christina Brandt

Department of Mathematics, Universität Hamburg, Germany

## Abstract

Magnetic particle imaging is a relatively new tracer-based medical imaging technique exploiting the non-linear magnetization response of magnetic nanoparticles to changing magnetic fields. If the data are generated by using a field-free line, the sampling geometry resembles the one in computerized tomography. Indeed, for an ideal field-free line rotating only in between measurements it was shown that the signal equation can be written as a convolution with the Radon transform of the particle concentration. In this work, we regard a continuously rotating field-free line and extend the forward operator accordingly. We obtain a similar result for the relation to the Radon data but with two additive terms resulting from the additional time-dependencies in the forward model. We jointly reconstruct particle concentration and corresponding Radon data by means of total variation regularization yielding promising results for synthetic data.

## 1 Introduction

Reliable and fast medical imaging techniques are indispensable for diagnostics in clinical everyday life. One promising example is magnetic particle imaging (MPI) invented by Gleich and Weizenecker [8]. MPI is a tracer-based imaging modality aiming for the reconstruction of the spatial distribution of magnetic nanoparticles injected into the patient's body. For data generation changing magnetic fields are applied to the field of view (FOV). These fields are composed of a selection field  $\mathbf{H}_S$  featuring a low-field volume (LFV), and a drive field  $\mathbf{H}_D$  moving the LFV through the FOV. The particles' corresponding non-linear magnetization response is measured in terms of induced voltages via receive coils. Note that only particles within the LFV contribute to the signal as all other particles stay in magnetic saturation, guaranteeing spatial information to be encoded in the data. The LFV takes different shapes depending on the specific scanner implementation. Most commonly, a field-free point (FFP) is used for spatial encoding. However, alternatively a field-free line (FFL) can be used as it was first suggested by [27]. For a detailed introduction to MPI, we recommend to consult [17]. For the specific case of an FFL scanner we further refer to [4] and [7].

For the remainder, we restrict ourselves towards the FFL encoding scheme. The first FFL imaging systems were developed by [9] and [3]. For further steps and breakthroughs in MPI history we refer to [19]. In [20] the open-source project OS-MPI is presented. Thereby, information about a small-bore FFL imager is shared. Advantages of using an FFL scanner lie in a possible increase in sensitivity [27] as more particles are contributing to the signal.

---

\*stephanie.blanke@uni-hamburg.de

Further, in [15] it is stated that using an FFL may lead to a less ill-posed problem compared to the FFP scanner.

During data acquisition the FFL is rotated and translated through the FOV resulting in scanning geometries resembling those in computerized tomography (CT). In CT the intensity loss of X-rays traversing the object under investigation is measured. Having access to data for a suitable choice of different positions for radiation source and detector panel, the attenuation coefficient of the specimen can be reconstructed. The forward operator is given by the Radon transform mapping a function to the set of its line integrals. See e.g. [22] for more information concerning CT. Since only particles in close vicinity to the FFL contribute to the induced voltage, it stands to reason that the MPI signal equation is linked to the Radon transform of the particle concentration. Indeed, it was shown in [18] that MPI data can be traced back to the Radon transform of the particle concentration. In [5] a similar result was derived using their newly developed 3D model applicable to magnetic fields approximately parallel to their velocity field. Hence, for concentration reconstruction, results and methods from the well-known imaging technique CT are accessible. Because of the aforementioned analogies, the idea aroused to combine the MPI with a CT scanner, thus combining quantitative information about the tracer distribution with structural information about the tissue itself. The first hybrid MPI-CT scanner was proposed in [25].

For the derivation of the relation between Radon and MPI data in [18], the FFL is assumed to be rotated in between measurements. In this work, we will use a slightly different scanning geometry, allowing the FFL to be rotated simultaneously with its translation as presented in the initial publication with respect to MPI using a field-free line [27]. In [5] and [18] it was proposed that the derived relation is still applicable in case that the rotation is sufficiently slow compared to the translation speed. In the remainder sections, we will investigate the supposition in some more details.

Throughout the article we will apply the Langevin theory to model the forward operator. This corresponds to assuming the particles to be in thermal equilibrium [17]. While being not a proper description of the particle dynamics, it is still the state of the art approach when using a model-based formulation of the signal equation. Alternatively, commonly a measurement-based approach is applied, where, before the actual data generation takes place, measurements are taken for a small probe being moved through the FOV called calibration process [17]. However, in recent years the problem of finding more accurate modeling methods aroused further interest, cf. ([16], [13], [26]) to name a few examples. In [13] e.g. the modeling task was traced back to an inverse parameter identification problem. In [14] a survey regarding mathematical modeling of the signal chain is given.

Finally, inspired by [24] we propose an image reconstruction approach, which jointly solves for the particle concentration as well as its corresponding Radon data by means of total variation (TV) regularization. Utilizing TV-based methods has a broad range of applications and is especially suitable for piecewise constant functions. See e.g. [6] for an introduction to TV regularization. Also in the setting of MPI TV has already been applied ([23], [28], [2]). In [12] the system-based approach combined with TV regularization has been compared with the projection-based approach using the Radon transform for an ideal FFL setup.

The article is organized as follows: In Section 2 we fix notation, introduce the MPI forward model for an FFL scanner, and review the link between MPI data and Radon transform of the particle concentration developed in [18]. Section 3 extends this relation to the setting of simultaneous line rotation. In Section 4 we propose a joint reconstruction of particle concentration and corresponding Radon data applying TV regularization. We close with numerical examples for synthetic data in Section 5.

## 2 Field-free Line Magnetic Particle Imaging

According to [17] the particle concentration  $c : \mathbb{R}^3 \rightarrow \mathbb{R}_0^+ := \mathbb{R}^+ \cup \{0\}$  can be linked to the voltage signal  $u_l : \mathbb{R}^+ \rightarrow \mathbb{R}$ ,  $l \in \{1, \dots, L\}$  induced in the  $l$ -th receive coil via

$$u_l(t) = -\mu_0 \int_{\mathbb{R}^3} c(\mathbf{r}) \frac{\partial}{\partial t} \bar{\mathbf{m}}(\mathbf{r}, t) \cdot \mathbf{p}_l(\mathbf{r}) \, d\mathbf{r}. \quad (1)$$

Thereby,  $\mu_0$  denotes the magnetic permeability,  $\bar{\mathbf{m}} : \mathbb{R}^3 \times \mathbb{R}^+ \rightarrow \mathbb{R}^3$  the mean magnetic moment, and  $\mathbf{p}_l : \mathbb{R}^3 \rightarrow \mathbb{R}^3$  the receive coil sensitivities. Note that we omit signal filtering. In practice, the direct feed-through of the excitation signal needs to be removed. In the following, we will assume that  $c$  and  $\frac{\partial}{\partial t} \bar{\mathbf{m}}(\cdot, t) \cdot \mathbf{p}_l(\cdot)$  are  $L_2$  functions, i.e. square-integrable. Thus, (1) is well-defined. When the field-free region of the MPI implementation is a straight line and the magnetic fields are constant along lines parallel to this FFL, it is called ideal FFL scanner. The attribute *ideal* is added as in practice we are confronted with field imperfections leading to deformed LFVs ([4], [5]). In the following, we consider an ideal FFL scanner generating data for different positions and directions by moving the FFL through the xy-plane. For convenience, we will assume the particle concentration to be contained within this plane and regard the problem as two dimensional  $c : \mathbb{R}^2 \rightarrow \mathbb{R}_0^+$  (cf. [15] for more details). Further, let  $\text{supp}(c) \subset B_R \subset \mathbb{R}^2$  with  $B_R$  denoting the circle of radius  $R > 0$  around the origin. Corresponding to [18] we model the magnetic fields as

$$\mathbf{H}(\mathbf{r}, \varphi, t) = \mathbf{H}_S(\mathbf{r}, \varphi) + \mathbf{H}_D(\varphi, t) = (-G \mathbf{r} \cdot \mathbf{e}_\varphi + A\Lambda(t)) \mathbf{e}_\varphi \quad (2)$$

with  $\mathbf{e}_\varphi := (-\sin \varphi, \cos \varphi)^T$ . Here,  $G$  is the gradient strength determining the width of the LFV,  $A$  denotes the drive peak amplitude, and  $\Lambda$  is a periodic excitation function usually chosen to be sinusoidal. A simple computation shows that the FFL which is orthogonal to  $\mathbf{e}_\varphi$  and with displacement  $s_t := \frac{A}{G} \Lambda(t)$  to the origin builds the center of the LFV

$$\text{FFL}(\mathbf{e}_\varphi, s_t) := \{ \mathbf{r} \in \mathbb{R}^2 : \mathbf{r} \cdot \mathbf{e}_\varphi = s_t \}. \quad (3)$$

The corresponding geometry is depicted in Figure 1. Looking at this visualization, by replacing the FFL with X-rays, similarities between the scanning process for MPI using an FFL scanner and the well-known medical imaging technique CT become obvious. Note that, as it was already mentioned in [18], when comparing with the notation in common CT literature  $\varphi$  needs to be shifted by  $\frac{\pi}{2}$ . This is because in CT the angle is usually measured from the axis to the orthogonal vector  $\mathbf{e}_\varphi$  instead to the X-ray itself.

Following [18] the mean magnetic moment can be rewritten using the Langevin model of paramagnetism

$$\bar{\mathbf{m}}(\mathbf{r}, \varphi, t) = \bar{m}(\|\mathbf{H}(\mathbf{r}, \varphi, t)\|) \frac{\mathbf{H}(\mathbf{r}, \varphi, t)}{\|\mathbf{H}(\mathbf{r}, \varphi, t)\|}$$

with  $\bar{m}(H) = m\mathcal{L}\left(\frac{\mu_0 m}{k_B T} H\right)$  denoting the modulus of the mean magnetic moment. Further,  $m$  is the magnetic moment of a single particle,  $k_B$  is the Boltzmann constant,  $T$  the particle temperature, and  $\mathcal{L} : \mathbb{R} \rightarrow [-1, 1]$  the Langevin function defined as

$$\mathcal{L}(\lambda) := \begin{cases} \coth(\lambda) - \frac{1}{\lambda} & , \lambda \neq 0, \\ 0 & , \lambda = 0. \end{cases} \quad (4)$$

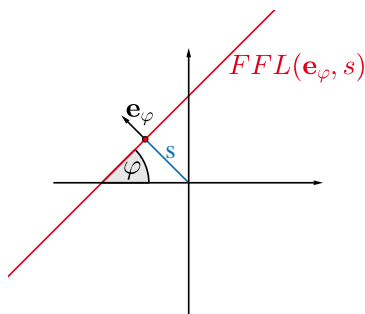


Figure 1: Visualization of the FFL orthogonal to  $\mathbf{e}_\varphi$  and with displacement  $s$  to the origin.

Thus,  $\bar{m}(-H) = -\bar{m}(H)$  and the signal equation (1) can be written as

$$u_l(\varphi, t) = -\mu_0 \int_{\mathbb{R}^2} c(\mathbf{r}) \frac{\partial}{\partial t} \bar{m}(-G \mathbf{r} \cdot \mathbf{e}_\varphi + A\Lambda(t)) \mathbf{e}_\varphi \cdot \mathbf{p}_l(\mathbf{r}) \, d\mathbf{r}. \quad (5)$$

Different scanning geometries exist. We regard *sequential line rotation* (Figure 2a) i.e. the FFL is sequentially translated through the FOV and rotated in between measurements, and *simultaneous line rotation* (Figure 2b) i.e. the FFL is rotated simultaneously to the translation (cf. [27], [18]). In the case of simultaneous line rotation we need to replace  $\varphi$  via  $\varphi_t := 2\pi f_{\text{rot}} t$  with line rotation frequency  $f_{\text{rot}} > 0$  everywhere  $\varphi$  occurs [5].

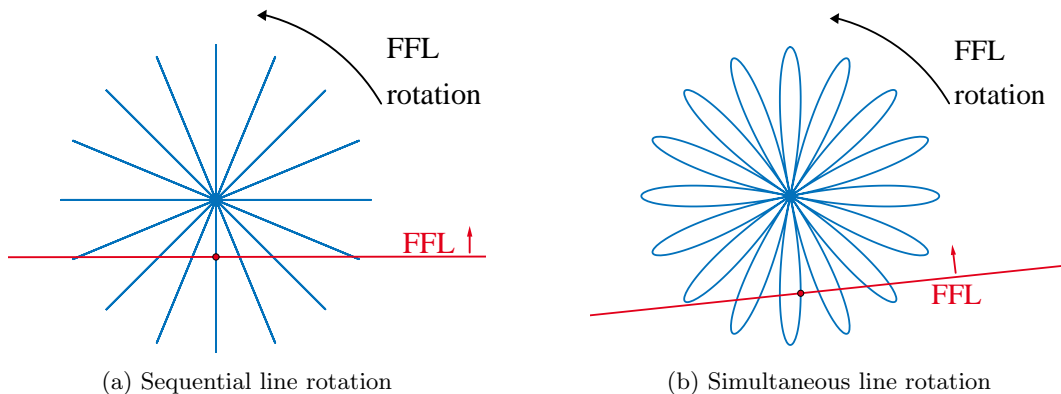


Figure 2: Different scanning geometries: (a) Sequential translation and rotation of the FFL, (b) Simultaneous translation and rotation of the FFL.

We now review the definition of the Radon transform. Let  $S^1$  be the unit sphere in  $\mathbb{R}^2$  and  $Z := S^1 \times [-R, R]$ . The Radon transform  $\mathcal{R} : L_2(B_R, \mathbb{R}_0^+) \rightarrow L_2(Z, \mathbb{R}_0^+)$  of the particle concentration  $c$  is given as

$$\mathcal{R}c(\mathbf{e}_\varphi, s) = \int_{B_R} c(\mathbf{r}) \delta(\mathbf{r} \cdot \mathbf{e}_\varphi - s) \, d\mathbf{r}. \quad (6)$$

For sequential line rotation a link between MPI data and the Radon transform of the particle concentration was shown (see Theorem 2.1 below).

**Theorem 2.1** [18] *Given spatially homogeneous receive coil sensitivities, sequential line rotation, and ideal magnetic fields, the signal equation (5) can be written as*

$$u_l(\varphi, t) = -\mu_0 A \Lambda'(t) \mathbf{e}_\varphi \cdot \mathbf{p}_l [\overline{m}'(G \cdot) * \mathcal{R}c(\mathbf{e}_\varphi, \cdot)] \left( \frac{A}{G} \Lambda(t) \right). \quad (7)$$

For simultaneous line rotation it is reasonably proposed that (7) holds approximately true as long as the FFL rotation is sufficiently slow compared to the translation ([18], [5]). The aim of this article is to investigate the setting of simultaneous line rotation in more detail. To this end, we define the MPI forward operator for the special case of ideal FFL scanner.

**Definition 2.2** *Let  $\mathcal{A}_l^{\text{FFL}} : L_2(B_R, \mathbb{R}_0^+) \rightarrow L_2(\mathbb{R}^+, \mathbb{R})$  be defined as*

$$\mathcal{A}_l^{\text{FFL}} c(t) := -\mu_0 \int_{B_R} c(\mathbf{r}) \frac{\partial}{\partial t} \overline{m}(-G \mathbf{r} \cdot \mathbf{e}_{\varphi_t} + A \Lambda(t)) \mathbf{e}_{\varphi_t} \cdot \mathbf{p}_l(\mathbf{r}) \, d\mathbf{r}. \quad (8)$$

*Then, for ideal magnetic fields, the mapping  $\mathcal{A}^{\text{FFL}} : L_2(B_R, \mathbb{R}_0^+) \rightarrow L_2(\mathbb{R}^+, \mathbb{R}^L)$  with  $\mathcal{A}^{\text{FFL}} c(t) = (\mathcal{A}_l^{\text{FFL}} c(t))_{l=1, \dots, L}$  is the forward operator for field-free line magnetic particle imaging.*

**Remark 2.3** *Note that, by choosing  $\varphi_t$  to be piecewise constant, sequential line rotation is also contained in the previous definition.*

For concentration reconstruction we need to solve the linear ill-posed inverse problem

$$\mathcal{A}^{\text{FFL}} c = \mathbf{u}$$

with measured data  $\mathbf{u} = (u_l)_{l=1, \dots, L}$  and forward operator  $\mathcal{A}^{\text{FFL}}$ .

### 3 Relation of the MPI Forward Operator to the Radon Transform

In the following, we examine the MPI forward operator in the ideal FFL setting for simultaneous line rotation. Therefore, let

$$\mathbf{R}^\varphi = \begin{pmatrix} \cos \varphi & -\sin \varphi \\ \sin \varphi & \cos \varphi \end{pmatrix}, \quad \mathbf{e}_\varphi = \begin{pmatrix} -\sin \varphi \\ \cos \varphi \end{pmatrix}, \quad \mathbf{e}_\varphi^\perp = -\begin{pmatrix} \cos \varphi \\ \sin \varphi \end{pmatrix}.$$

Further, we define a weighted Radon transform

$$\widetilde{\mathcal{R}}c(\mathbf{e}_\varphi, s) := \int_{B_R} c(\mathbf{r}) \delta(\mathbf{r} \cdot \mathbf{e}_\varphi - s) \mathbf{r} \cdot \mathbf{e}_\varphi^\perp \, d\mathbf{r}. \quad (9)$$

The next theorem states a link between the MPI forward operator (8), the Radon transform (6), and the weighted Radon transform (9).

**Theorem 3.1** *Given spatially homogeneous receive coil sensitivities, simultaneous line rotation, and ideal magnetic fields, the MPI forward operator with respect to the  $l$ -th receive coil can be written as*

$$\mathcal{A}_l^{\text{FFL}} = \mathcal{K}_{1,l} \circ \mathcal{R} + \mathcal{K}_{2,l} \circ \widetilde{\mathcal{R}} + \mathcal{K}_{3,l} \circ \mathcal{R}$$

with convolution operators  $\mathcal{K}_{i,l} : L_2(Z, \mathbb{R}) \rightarrow L_2(\mathbb{R}^+, \mathbb{R})$  for  $i = 1, 2, 3$  and  $l \in \{1, \dots, L\}$

$$\begin{aligned}\mathcal{K}_{1,l}f(t) &= -\mu_0 A\Lambda'(t) \mathbf{e}_{\varphi_t} \cdot \mathbf{p}_l \bar{m}'(G \cdot) * f(\mathbf{e}_{\varphi_t}, \cdot)(s_t), \\ \mathcal{K}_{2,l}f(t) &= \mu_0 G\varphi'_t \mathbf{e}_{\varphi_t} \cdot \mathbf{p}_l \bar{m}'(G \cdot) * f(\mathbf{e}_{\varphi_t}, \cdot)(s_t), \\ \mathcal{K}_{3,l}f(t) &= -\mu_0 \varphi'_t \mathbf{e}_{\varphi_t}^\perp \cdot \mathbf{p}_l \bar{m}(G \cdot) * f(\mathbf{e}_{\varphi_t}, \cdot)(s_t).\end{aligned}$$

**Proof:** Computing the derivative in (8) and assuming spatially homogeneous receive coil sensitivities we obtain

$$\begin{aligned}\mathcal{A}_l^{\text{FFL}}c(t) &= -\mu_0 A\Lambda'(t) \mathbf{e}_{\varphi_t} \cdot \mathbf{p}_l \int_{B_R} c(\mathbf{r}) \bar{m}'(-G \mathbf{r} \cdot \mathbf{e}_{\varphi_t} + A\Lambda(t)) d\mathbf{r} \\ &+ \mu_0 G\varphi'_t \mathbf{e}_{\varphi_t} \cdot \mathbf{p}_l \int_{B_R} c(\mathbf{r}) \bar{m}'(-G \mathbf{r} \cdot \mathbf{e}_{\varphi_t} + A\Lambda(t)) \mathbf{r} \cdot \mathbf{e}_{\varphi_t}^\perp d\mathbf{r} \\ &- \mu_0 \varphi'_t \mathbf{e}_{\varphi_t}^\perp \cdot \mathbf{p}_l \int_{B_R} c(\mathbf{r}) \bar{m}(-G \mathbf{r} \cdot \mathbf{e}_{\varphi_t} + A\Lambda(t)) d\mathbf{r},\end{aligned}$$

where we used  $(\mathbf{e}_{\varphi_t})' = \varphi'_t \mathbf{e}_{\varphi_t}^\perp$ . We proceed similar to [18] and rotate the coordinate system  $\mathbf{r}' := \mathbf{R}^{-\varphi_t} \mathbf{r}$  such that the x-axis gets parallel to the FFL. Using

$$\mathbf{R}^{\varphi_t} \mathbf{r}' = \mathbf{R}^{\varphi_t} \begin{pmatrix} v' \\ s' \end{pmatrix} = s' \mathbf{e}_{\varphi_t} - v' \mathbf{e}_{\varphi_t}^\perp$$

yields

$$\begin{aligned}\text{FFL}(\mathbf{e}_{\varphi_t}, s') &= \{\mathbf{r} \in \mathbb{R}^2 : \mathbf{r} \cdot \mathbf{e}_{\varphi_t} = s'\} = \{s' \mathbf{e}_{\varphi_t} - v' \mathbf{e}_{\varphi_t}^\perp : v' \in \mathbb{R}\} \\ &= \left\{ \mathbf{R}^{\varphi_t} \begin{pmatrix} v' \\ s' \end{pmatrix} : v' \in \mathbb{R} \right\}\end{aligned}$$

and with  $\mathbf{R}^{-\varphi_t} B_R = B_R$  we obtain

$$\begin{aligned}\mathcal{A}_l^{\text{FFL}}c(t) &= -\mu_0 A\Lambda'(t) \mathbf{e}_{\varphi_t} \cdot \mathbf{p}_l \int_{\mathbb{R}} \mathcal{R}c(\mathbf{e}_{\varphi_t}, s') \bar{m}'(-G s' + A\Lambda(t)) ds' \\ &+ \mu_0 G\varphi'_t \mathbf{e}_{\varphi_t} \cdot \mathbf{p}_l \int_{\mathbb{R}} \tilde{\mathcal{R}}c(\mathbf{e}_{\varphi_t}, s') \bar{m}'(-G s' + A\Lambda(t)) ds' \\ &- \mu_0 \varphi'_t \mathbf{e}_{\varphi_t}^\perp \cdot \mathbf{p}_l \int_{\mathbb{R}} \mathcal{R}c(\mathbf{e}_{\varphi_t}, s') \bar{m}(-G s' + A\Lambda(t)) ds'.\end{aligned}$$

Hence, we finally get

$$\mathcal{A}_l^{\text{FFL}} = \mathcal{K}_{1,l} \circ \mathcal{R} + \mathcal{K}_{2,l} \circ \tilde{\mathcal{R}} + \mathcal{K}_{3,l} \circ \mathcal{R}$$

completing the proof.  $\square$

**Remark 3.2** The operators  $\mathcal{K}_{2,l}$  and  $\mathcal{K}_{3,l}$  result from the extra derivatives, due to the additional time dependencies in (8) for simultaneous line rotation. For sequential line rotation these terms vanish as we choose  $\varphi_t$  to be piecewise constant and Theorem 3.1 reduces to Theorem 2.1.

**Remark 3.3** Regarding an oscillating non-rotating FFL with a phantom continuously rotating in opposite direction to the FFL rotation in the simultaneous setting, we would obtain

$$\mathcal{A}_l^{\text{FFL}} = \mathcal{K}_{1,l} \circ \mathcal{R} + \mathcal{K}_{2,l} \circ \tilde{\mathcal{R}}$$

as forward operator. For simultaneous line rotation the term  $\mathcal{K}_{3,l}$  results from the temporal change of the magnetic field orientation with respect to the receive coils sensitivity  $\mathbf{p}_l$  and thus, is not present in the just considered case.

Since the two additional terms scale with the FFL rotation speed, we assume, as proposed in ([5], [18]), that Theorem 2.1 can still be used in case  $\varphi'_t$  is suitably small. To further confirm this, we conclude this section by deriving upper bounds for  $|\mathcal{K}_{2,l}\tilde{\mathcal{R}}c(t)|$  respectively  $|\mathcal{K}_{3,l}\mathcal{R}c(t)|$ .

**Lemma 3.4** *Let  $R = \frac{\Delta}{G}$ , i.e. we suppose that the particle concentration is completely located within the sampling region as usually  $\frac{\Delta}{G}$  is the maximum displacement of the FFL. Then, we have that*

$$|\mathcal{K}_{1,l}\mathcal{R}c(t)| \geq \frac{|\Lambda'(t)|}{\varphi'_t} |\mathcal{K}_{2,l}\tilde{\mathcal{R}}c(t)|.$$

**Proof:** It holds for  $(\mathbf{e}_\varphi, s) \in Z$  that

$$\begin{aligned} \tilde{\mathcal{R}}c(\mathbf{e}_\varphi, s) &= \int_{B_R} c(\mathbf{r}) \delta(\mathbf{r} \cdot \mathbf{e}_\varphi - s) \mathbf{r} \cdot \mathbf{e}_\varphi^\perp d\mathbf{r} \\ &= - \int_{-\sqrt{R^2-s^2}}^{\sqrt{R^2-s^2}} c(s \mathbf{e}_\varphi - v \mathbf{e}_\varphi^\perp) v dv \leq R \mathcal{R}c(\mathbf{e}_\varphi, s). \end{aligned}$$

Hence, we get

$$\begin{aligned} |\mathcal{K}_{1,l}\mathcal{R}c(t)| &= |\mu_0 A \Lambda'(t) \mathbf{e}_{\varphi_t} \cdot \mathbf{p}_l \bar{m}'(G \cdot) * \mathcal{R}c(\mathbf{e}_{\varphi_t}, \cdot)(s_t)| \\ &= |\mu_0 G R \Lambda'(t) \mathbf{e}_{\varphi_t} \cdot \mathbf{p}_l \bar{m}'(G \cdot) * \mathcal{R}c(\mathbf{e}_{\varphi_t}, \cdot)(s_t)| \\ &\geq \left| \mu_0 G \Lambda'(t) \mathbf{e}_{\varphi_t} \cdot \mathbf{p}_l \bar{m}'(G \cdot) * \tilde{\mathcal{R}}c(\mathbf{e}_{\varphi_t}, \cdot)(s_t) \right| \\ &= \left| \frac{\Lambda'(t)}{\varphi'_t} \mu_0 G \varphi'_t \mathbf{e}_{\varphi_t} \cdot \mathbf{p}_l \bar{m}'(G \cdot) * \tilde{\mathcal{R}}c(\mathbf{e}_{\varphi_t}, \cdot)(s_t) \right| \\ &= \frac{|\Lambda'(t)|}{\varphi'_t} |\mathcal{K}_{2,l}\tilde{\mathcal{R}}c(t)|. \end{aligned}$$

□

The ratio in the last lemma relates the FFL translation with the rotation speed and thus, if it is sufficiently large,  $\mathcal{K}_{2,l}\tilde{\mathcal{R}}c(t)$  might be neglected in the image reconstruction process. As already mentioned, usually the excitation function is chosen to be sinusoidal, e.g.  $\Lambda(t) = -\cos(2\pi f_d t)$ , with drive frequency  $f_d > 0$ . Then, we get that

$$\frac{|\Lambda'(t)|}{\varphi'_t} = \frac{f_d}{f_{\text{rot}}} |\sin(2\pi f_d t)|. \quad (10)$$

At each turning point of the FFL the first term  $\mathcal{K}_{1,l}\mathcal{R}c$  becomes zero. By (10) the time intervals, in which the second term  $\mathcal{K}_{2,l}\tilde{\mathcal{R}}c$  might overweight the first integral, are the smaller the larger the ratio  $\frac{f_d}{f_{\text{rot}}}$  gets. According to [26] drive frequencies are around 1 kHz to 150 kHz. A typical upper bound for the rotation frequency is 100 Hz [5] leading to  $\frac{f_d}{f_{\text{rot}}} \geq 10$ . At last, we state an example of particle concentrations leading to a vanishing  $\mathcal{K}_{2,l}\tilde{\mathcal{R}}c$ .

**Example 3.5** Let  $c$  be radial symmetric, i.e.  $c(\mathbf{r}) = c(|\mathbf{r}|)$ . We compute

$$-\tilde{\mathcal{R}}c(\mathbf{e}_\varphi, s) = \int_{-\sqrt{R^2-s^2}}^{\sqrt{R^2-s^2}} c(s \mathbf{e}_\varphi - v \mathbf{e}_\varphi^\perp) v \, dv = \int_{-\sqrt{R^2-s^2}}^{\sqrt{R^2-s^2}} c\left(\sqrt{s^2+v^2}\right) v \, dv = 0.$$

Next, we give an estimate for the third integral  $\mathcal{K}_{3,l}\mathcal{R}c(t)$ .

**Lemma 3.6** With  $m$  denoting the magnetic moment of a single particle and  $N_p$  the total amount of particles contained in the tracer injection, it holds that

$$|\mathcal{K}_{3,l}\mathcal{R}c(t)| \leq \mu_0 \varphi'_t \|\mathbf{p}_l\| m N_p.$$

**Proof:** According to the proof of Theorem 3.1 we have

$$|\mathcal{K}_{3,l}\mathcal{R}c(t)| = \left| \mu_0 \varphi'_t \mathbf{e}_{\varphi_t}^\perp \cdot \mathbf{p}_l \int_{B_R} c(\mathbf{r}) \overline{m} (-G \mathbf{r} \cdot \mathbf{e}_{\varphi_t} + A\Lambda(t)) \, d\mathbf{r} \right|.$$

The modulus of the mean magnetic moment is bounded by  $m$  (cf. Langevin model in Section 2) yielding

$$|\mathcal{K}_{3,l}\mathcal{R}c(t)| \leq \left| \mu_0 \varphi'_t \mathbf{e}_{\varphi_t}^\perp \cdot \mathbf{p}_l m \int_{B_R} c(\mathbf{r}) \, d\mathbf{r} \right| \leq \mu_0 \varphi'_t \|\mathbf{p}_l\| m N_p.$$

□

**Remark 3.7** For practical reasons it might be convenient to state an upper bound in terms of the maximal particle concentration  $c_{\max}$ . This can be easily obtained by using  $N_p \leq c_{\max} \pi R^2$ .

In case the phantom is fully located within the saturation area on one side of the FFL, the above inequality holds approximately with equality. The estimate in the last Lemma can be computed beforehand to measurements as all components are determined by the scanner setup and the choice of the injected tracer. Thus, this upper bound can be determined and compared to the magnitudes of measured data in order to evaluate whether incorporation is needed. From the  $s$ -shape of the Langevin function it follows that  $|\mathcal{K}_{3,l}\mathcal{R}c(t)|$  is largest at turning points of the FFL, which are the zero crossings of  $|\mathcal{K}_{1,l}\mathcal{R}c(t)|$ .

## 4 TV regularized Image Reconstruction

Inspired by [24] we reconstruct particle concentration and Radon data simultaneously via total variation regularization. To this end, we first introduce the space of functions of bounded variation BV on the domain  $B_R$

$$\text{BV}(B_R) := \{c \in L_1(B_R, \mathbb{R}) : \text{TV}(c) < \infty\},$$

with

$$\text{TV}(c) := \sup \left\{ \int_{\mathbb{R}^2} c(\mathbf{r}) \operatorname{div}(\mathbf{g})(\mathbf{r}) \, d\mathbf{r} : \mathbf{g} \in C_0^\infty(B_R, \mathbb{R}^2), |\mathbf{g}(\mathbf{r})|_2 < 1 \text{ for all } \mathbf{r} \right\}.$$



Equipped with the norm  $\|\cdot\|_{\text{BV}} := \|\cdot\|_{L_1} + \text{TV}(\cdot)$  this space becomes a Banach space and it holds  $\text{BV}(B_R) \subset L_2(B_R, \mathbb{R})$ . Additionally, the Poincaré-Wirtinger inequality holds

$$\|c - \bar{c}\|_{L_2} \leq C \text{TV}(c), \quad \bar{c} = \frac{1}{\pi R^2} \int_{B_R} c(\mathbf{r}) \, d\mathbf{r} \quad (11)$$

for some constant  $C > 0$ . For more information concerning TV we recommend to consult e.g. [1] and [6].

Define  $\mathcal{D} := L_2(B_R, \mathbb{R}) \times L_2(Z, \mathbb{R})$  and let  $A_l : \mathcal{D} \rightarrow L_2(\mathbb{R}^+, \mathbb{R})$  such that

$$A_l(c, v) := \mathcal{K}_{1,l}v + \left(\mathcal{K}_{2,l} \circ \tilde{\mathcal{R}}\right)c + \mathcal{K}_{3,l}v \quad (12)$$

with operators  $\mathcal{K}_{i,l}$ ,  $i = 1, 2, 3$  defined in Theorem 3.1. It holds that  $A_l(c, \mathcal{R}c) = \mathcal{A}_l^{\text{FFL}}c$  for  $c \geq 0$ . Now, we are able to state the minimization problem we want to solve

$$\min_{(c,v) \in \mathcal{C}} \frac{1}{2} \sum_l \|A_l(c, v) - u_l\|_{L_2}^2 + \frac{\alpha_1}{2} \|\mathcal{R}c - v\|_{L_2}^2 + \alpha_2 \text{TV}(c), \quad (13)$$

with feasible set  $\mathcal{C} := \{(c, v) \in \mathcal{D} : c \geq 0, v \geq 0\}$ , given data  $u_l$ ,  $l = 1, \dots, L$ , weighting parameter  $\alpha_1$ , and regularization parameter  $\alpha_2 > 0$ . Note that actively we only penalize the choice of the particle concentration. Nevertheless, if needed an additional regularization term acting on the Radon data  $v$  can be included, e.g. directional TV regularization as used in [24].

**Theorem 4.1** *The minimization problem (13) has a solution  $(c^*, v^*) \in \mathcal{C}$  and  $c^* \in \text{BV}(B_R)$ .*

**Proof:** Rewriting the constrained optimization problem (13) using the indicator function  $\delta_{\mathcal{C}}$  yields

$$\begin{aligned} & \min_{(c,v) \in \mathcal{D}} J(c, v), \\ J(c, v) & := \frac{1}{2} \sum_l \|A_l(c, v) - u_l\|_{L_2}^2 + \frac{\alpha_1}{2} \|\mathcal{R}c - v\|_{L_2}^2 + \alpha_2 \text{TV}(c) + \delta_{\mathcal{C}}(c, v). \end{aligned}$$

Note that  $\mathcal{D}$  is a Hilbertspace with inner product

$$\langle \cdot, \cdot \rangle_{\mathcal{D}} := \langle \cdot, \cdot \rangle_{L_2(B_R, \mathbb{R})} + \langle \cdot, \cdot \rangle_{L_2(Z, \mathbb{R})}.$$

Obviously  $J$  is proper. The total variation  $\text{TV}(c)$  is convex and weakly lower semicontinuous according to [1]. Further,  $A_l$  and  $\mathcal{R}$  are linear bounded operators and the feasible set  $\mathcal{C}$  is closed and convex. Thus,  $J$  is jointly convex in  $(c, v)$  and weakly lower semicontinuous. For existence the only remaining part to show is that  $J$  is also coercive. From [1] we know that

$$\|c\|_{\text{BV}} \rightarrow \infty \implies \frac{\alpha_1}{2} \|\mathcal{R}c - v\|_{L_2}^2 + \alpha_2 \text{TV}(c) \rightarrow \infty \quad (14)$$

as  $\mathcal{R}c$  does not annihilate for constant functions. Regard now

$$\|(c, v)\|_{\mathcal{D}}^2 = \|c\|_{L_2}^2 + \|v\|_{L_2}^2 \rightarrow \infty.$$

Then, either  $\|c\|_{L_2}$  or  $\|v\|_{L_2}$  needs to tend to infinity. If  $\|v\|_{L_2} \rightarrow \infty$  we directly get that  $J(c, v) \rightarrow \infty$  as  $\|\mathcal{R}c - v\|_{L_2}^2 \rightarrow \infty$ . Thus, we assume that  $\|v\|_{L_2}$  is bounded and  $\|c\|_{L_2} \rightarrow \infty$ .

From (11) we get with  $\mathbf{1}_{B_R}$  denoting the characteristic function

$$\begin{aligned} \|c\|_{L_2} &\leq \|c - \bar{c}\mathbf{1}_{B_R}\|_{L_2} + \|\bar{c}\mathbf{1}_{B_R}\|_{L_2} \leq C \text{TV}(c) + \sqrt{\pi R^2} |\bar{c}| \\ &= C \text{TV}(c) + \frac{1}{\sqrt{\pi R^2}} \|c\|_{L_1} \leq \max\left\{C, \frac{1}{\sqrt{\pi R^2}}\right\} \|c\|_{\text{BV}} \end{aligned}$$

and thus,  $\|c\|_{\text{BV}} \rightarrow \infty$  if  $\|c\|_{L_2} \rightarrow \infty$ . Together with (14) we finally obtain that  $J$  is coercive yielding existence of a minimizer.  $\square$

## 5 Numerical Results

Finally, we state numerical results for synthetic data. Thereby, the basis for our data simulation is given by the framework developed by Gael Bringout [4] available at <https://github.com/gBringout>. Accordingly, the tracer is modeled as a solution with  $0.5 \frac{\text{mol}(\text{Fe}_3\text{O}_4)}{\text{m}^3}$  concentration of magnetite with 30 nm core diameter and  $\frac{0.6}{\mu_0}$  T saturation magnetization. As excitation function we choose

$$\Lambda(t) = -\cos(2\pi f_d t) \quad (15)$$

with drive frequency  $f_d$ . Further parameters can be found in Table 1. Our concentration phantom (cf. Figure 4a) is normalized to one and located within a circle around the origin with radius  $\frac{A}{G}$ , which is the maximum displacement of the FFL. Thus, we set the FOV to be  $[-\frac{A}{G}, \frac{A}{G}] \times [-\frac{A}{G}, \frac{A}{G}]$ . For data generation we divide the FOV into  $501 \times 501$ , for image reconstruction into  $201 \times 201$  pixel. In case of sequential line rotation, we gather data for 25 sweeps of the FFL through the FOV and angles equally distributed in  $[0, \pi]$ . More precisely, we regard angles  $\varphi_j = (j-1) \frac{\pi}{25}$ ,  $j = 1, \dots, 25$ . Considering simultaneous line rotation, we choose a total measurement time of  $\frac{1}{2f_{\text{rot}}}$  resulting in the same amount of FFL translations through the phantom covering angles again in  $[0, \pi]$ .

Table 1: Simulation parameters

Parameter	Explanation	Value	Unit
$\mu_0$	magnetic permeability	$4\pi \cdot 10^{-7}$	$\text{TmA}^{-1}$
$k_B$	Boltzmann constant	$1.380650424 \cdot 10^{-23}$	$\text{JK}^{-1}$
$G$	gradient strength	4	$\text{T}(\text{m}\mu_0)^{-1}$
$A$	drive peak amplitude	15	$\text{mT}\mu_0^{-1}$
$\mathbf{p}_1$	sensitivity of the first receive coil	$[0.015/293.29, 0]^T$	
$\mathbf{p}_2$	sensitivity of the second receive coil	$[0, 0.015/379.71]^T$	
$f_d$	drive-field frequency	25	kHz
$f_{\text{rot}}$	line rotation frequency	1	kHz
$f_s$	sampling frequency	8	MHz

In the following, we denote

$$\widehat{\mathcal{K}}_{i,l}f(t) := \frac{\mathcal{K}_{i,l}f(t)}{\max_t \{|\mathcal{K}_{1,l}f(t)|\}}, \quad \text{for } i = 1, 2, 3, l = 1, 2.$$

For our reconstructions, we neglect the second term of the forward operator (12), which is justified due to Lemma 3.4 and the choice of frequencies. This is emphasized by Figure 3. The left plot shows  $\widehat{\mathcal{K}}_{1,1}\mathcal{R}c$  in comparison to  $\widehat{\mathcal{K}}_{3,1}\mathcal{R}c$ , whereas the right plot images  $\widehat{\mathcal{K}}_{2,1}\widetilde{\mathcal{R}}c + \widehat{\mathcal{K}}_{3,1}\mathcal{R}c$  and  $\widehat{\mathcal{K}}_{3,1}\mathcal{R}c$ . We find that both additional terms are small compared to  $\widehat{\mathcal{K}}_{1,1}\mathcal{R}c$ . Especially the second term seems to have only an influence, when the main part reaches its highest values, while the third term is largest for the zero crossings of  $\widehat{\mathcal{K}}_{1,1}\mathcal{R}c$ .

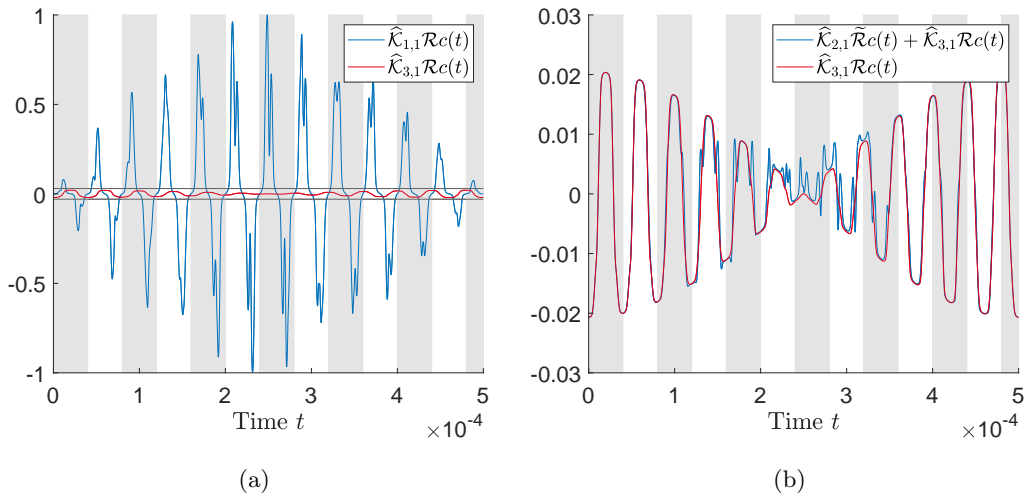


Figure 3: Plots showing  $\widehat{\mathcal{K}}_{1,1}\mathcal{R}c$  (blue) in comparison to  $\widehat{\mathcal{K}}_{3,1}\mathcal{R}c$  (red) together with the bound determined in Lemma 3.6 (dark grey) (a) and  $\widehat{\mathcal{K}}_{2,1}\widetilde{\mathcal{R}}c + \widehat{\mathcal{K}}_{3,1}\mathcal{R}c$  (blue) in comparison to  $\widehat{\mathcal{K}}_{3,1}\mathcal{R}c$  (red) (b) for the phantom in Figure 4a. Blocks in the background of the two plots demonstrate periods of the drive field. The total measurement time is  $12.5 \frac{1}{f_d} = \frac{1}{2f_{\text{rot}}}$ .

Figure 4a shows the phantom which we want to reconstruct. In order to evaluate the discretized version of (12) for a specific time point, the corresponding column in a sinogram filled angle by angle is needed. Thus, to be able to compute data for every sampling point, a sinogram containing a column for each angle the FFL attains during scanning is needed. For sequential line rotation this amounts to the sinogram shown in Figure 4b, for simultaneous line rotation to the one in Figure 5a. In order to reduce the problem size, we rather aim at reconstructing only the sinogram taking values along the dashed line in Figure 5a resulting in Figure 5b. Thereby, we get an additional error but because of the shape of the convolution kernel of the main part  $\widehat{\mathcal{K}}_{1,l}\mathcal{R}c$ , which converges to the dirac delta for particle diameters tending to infinity [17], and using a regularization method for reconstruction this should be no further problem.

We discretize (13) by applying standard methods. We define discretized versions of the Radon transform  $\mathbf{R}_{\text{seq}}$  and  $\mathbf{R}_{\text{sim}}$  such that  $\mathbf{R}_{\text{seq}}\mathbf{c}$  yields the sinogram in Figure 4b and  $\mathbf{R}_{\text{sim}}\mathbf{c}$  the one in Figure 5b. Further, we scale data  $\mathbf{u}_l$  and discretized forward operators  $\mathbf{K}_{i,l}$  by dividing by the maximum absolute data value  $u^*$

$$\widehat{\mathbf{u}}_l := \frac{\mathbf{u}_l}{u^*}, \quad \widehat{\mathbf{K}}_{i,l} := \frac{\mathbf{K}_{i,l}}{u^*}.$$

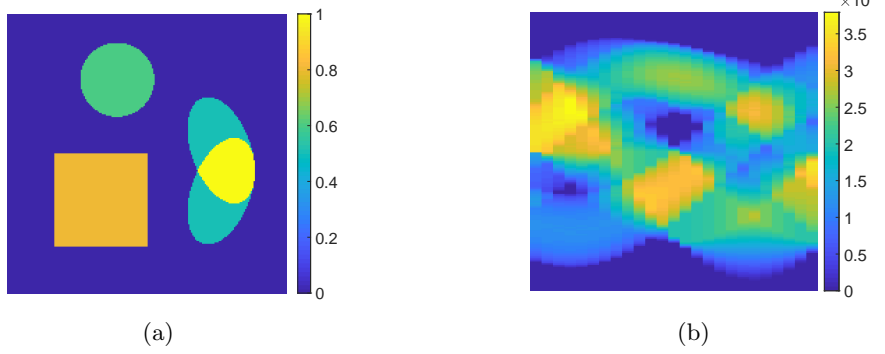


Figure 4: Phantom (a) and corresponding sinogram filled angle by angle (b).

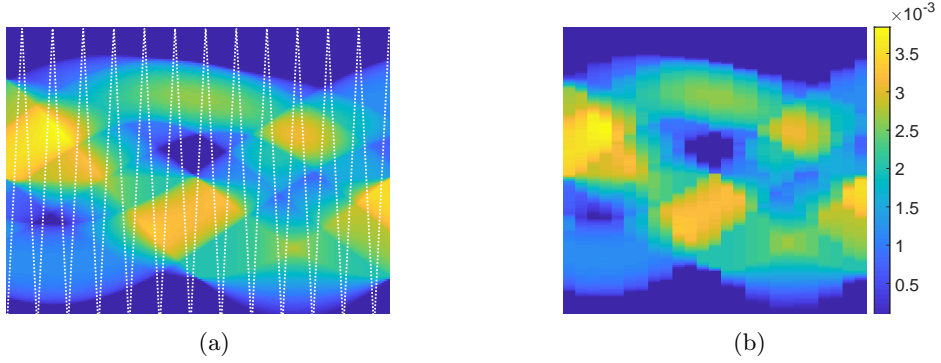


Figure 5: (a) Sinogram for the phantom shown in Figure 4a with columns for each angle attained by the FFL during scanning. (b) Adapted version filled following the dashed line in (a).

Table 2: Reconstruction methods

Method	Regarded minimization problem
$\mathcal{M}_1$	$\min_{\mathbf{c} \geq 0, \mathbf{v} \geq 0} \frac{1}{2} \sum_{l=1}^2 \left\  \widehat{\mathbf{K}}_{1,l} \mathbf{v} - \widehat{\mathbf{u}}_l \right\ _2^2 + \frac{\alpha_1}{2} \ \mathbf{R}_{\text{seq}} \mathbf{c} - \mathbf{v}\ _2^2 + \alpha_2 \ \nabla \mathbf{c}\ _2 \ _1$
$\mathcal{M}_2$	$\min_{\mathbf{c} \geq 0, \mathbf{v} \geq 0} \frac{1}{2} \sum_{l=1}^2 \left\  \widehat{\mathbf{K}}_{1,l} \mathbf{v} - \widehat{\mathbf{u}}_l \right\ _2^2 + \frac{\alpha_1}{2} \ \mathbf{R}_{\text{sim}} \mathbf{c} - \mathbf{v}\ _2^2 + \alpha_2 \ \nabla \mathbf{c}\ _2 \ _1$
$\mathcal{M}_3$	$\min_{\mathbf{c} \geq 0, \mathbf{v} \geq 0} \frac{1}{2} \sum_{l=1}^2 \left\  \left( \widehat{\mathbf{K}}_{1,l} + \widehat{\mathbf{K}}_{3,l} \right) \mathbf{v} - \widehat{\mathbf{u}}_l \right\ _2^2 + \frac{\alpha_1}{2} \ \mathbf{R}_{\text{sim}} \mathbf{c} - \mathbf{v}\ _2^2 + \alpha_2 \ \nabla \mathbf{c}\ _2 \ _1$

For reconstruction we regard the versions of (13) specified in Table 2. To solve the resulting problem, we use CVX, a package for specifying and solving convex programs ([11], [10]), together with the MOSEK solver [21]. For our weighting parameters we choose  $\alpha_1 \in \{1, 2, 4\} \cdot 10^4$  and  $\alpha_2 \in \{0.1^{5.5-i0.05}, i = 0, \dots, 49\}$  such that  $(\alpha_1, \alpha_2)$  maximizes the structural similarity (SSIM) of the reconstructed particle concentration with the groundtruth. However, there might be better parameter choices. Note that  $s_t$ , i.e. the distance of the FFL to the origin, is not sampled equidistantly due to the choice of the excitation function (15) and because we sample for equidistant time points (cf. [18]). While in [18] they need to process and regrid the signal to be able to use Wiener deconvolution, this is not necessary for our methods.

We start with a result for sequential line rotation in Figure 6. We obtain good reconstructions for both, the phantom as well as the Radon data. Nevertheless, the vertices of the square are not resolved a hundred percent properly. This is likely due to missing information in the data and because we used an isotropic version of the TV penalty term, which favors rounded edges (cf. [6]). Next, we regard results for the setting of simultaneous line

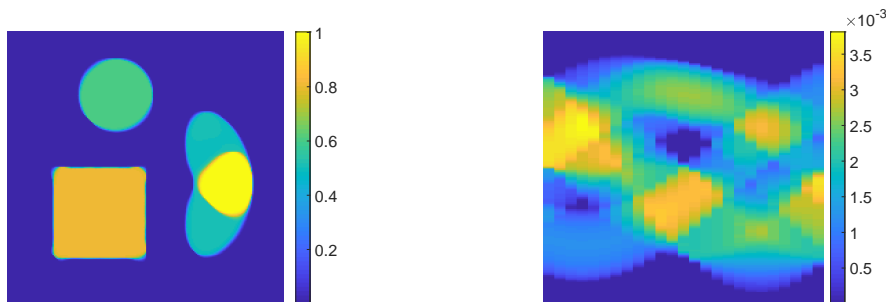


Figure 6: Reconstruction of phantom and sinogram for sequential line rotation via  $\mathcal{M}_1$ . ( $\alpha_1 = 2 \cdot 10^4$ ,  $\alpha_2 = 0.1^{5.1}$ ,  $\text{SSIM}(\mathbf{c}) = 0.9492$ )

rotation. Similar to [5], we get a slightly rotated version of the phantom when ignoring the different sampling pattern, see Figure 7.

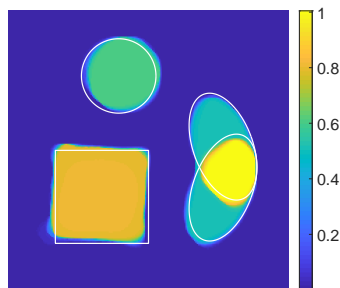


Figure 7: Phantom reconstruction for simultaneous line rotation using model  $\mathcal{M}_1$ , i.e. ignoring the specific sampling pattern for simultaneous line rotation. Contours of the groundtruth are depicted in white. ( $\alpha_1 = 4 \cdot 10^4$ ,  $\alpha_2 = 0.1^4$ ,  $\text{SSIM}(\mathbf{c}) = 0.7976$ )

Lastly, we compare reconstructions incorporating  $\mathcal{K}_{3,t}\mathcal{R}$  with those neglecting this term.

According to Figure 3b we expect only slight differences. Corresponding deliverables with and without added gaussian noise with  $2 \cdot 10^{-10}$  standard deviation (ca. 0.79% of  $u^*$ ) can be found in Figure 8. Our reconstructions show that incorporation of the third term in the model yields slightly higher values for structural similarity and for the noiseless case, the quantitative concentration values fit better to the groundtruth. For noisy data the size of  $\mathcal{K}_{3,l}\mathcal{R}$  gets close to the range of added noise and thus, it is reasonable that the gain in the SSIM value is lower compared to the noise-free setting.

## 6 Conclusion

In this work, we regarded the relation of MPI and Radon data for a continuously rotating FFL. Because of the time derivative in the signal equation and the additional time-dependencies for this setting, we get two additive terms in the forward model. We derived bounds for these two terms supporting the assumption of [5] and [18] that for sufficiently slow FFL rotation compared to the translation speed, the results from the sequential line rotation setting can be applied. This is also emphasized by our numerical results. Incorporation of the additional terms for image reconstruction does not seem to be necessary on a first view. However, including the third term in our reconstruction approach is simple because both terms together still form a convolution with the Radon data of the particle concentration. Further, its bound can be computed beforehand of reconstruction and thus, its magnitude can be compared to the total signal. In our case, incorporation yielded slightly better structural similarity values. Future research will comprise steps towards a more realistic set of assumptions, like time-dependent particle concentrations, magnetic field imperfections, and that the direct feedthrough of the excitation signal needs to be removed. Moreover, it would be interesting to extend the results of this article to different modeling approaches distinct from the Langevin model.

## Acknowledgment

The authors acknowledge the support by the Deutsche Forschungsgemeinschaft (DFG) within the Research Training Group GRK 2583 "Modeling, Simulation and Optimization of Fluid Dynamic Applications".

## References

- [1] Robert Acar and Curtis R Vogel. Analysis of bounded variation penalty methods for ill-posed problems. *Inverse problems*, 10(6):1217, 1994.
- [2] Christine Bathke, Tobias Kluth, Christina Brandt, and Peter Maaß. Improved image reconstruction in magnetic particle imaging using structural a priori information. *International Journal on Magnetic Particle Imaging*, 3(1), 2017.
- [3] Klaas Bente, Matthias Weber, Matthias Graeser, Timo F Sattel, Marlitt Erbe, and Thorsten M Buzug. Electronic field free line rotation and relaxation deconvolution in magnetic particle imaging. *IEEE transactions on medical imaging*, 34(2):644–651, 2014.
- [4] Gaël Bringout. *Field free line magnetic particle imaging: characterization and imaging device up-scaling*. PhD thesis, Dissertation, Lübeck, Universität zu Lübeck, 2016, 2016.

- [5] Gaël Bringout, Wolfgang Erb, and Jürgen Friel. A new 3d model for magnetic particle imaging using realistic magnetic field topologies for algebraic reconstruction. *Inverse Problems*, 36(12):124002, 2020.
- [6] Martin Burger and Stanley Osher. A guide to the TV zoo. In *Level set and PDE based reconstruction methods in imaging*, pages 1–70. Springer, 2013.
- [7] Marlitt Erbe. *Field free line magnetic particle imaging*. Springer Science & Business Media, 2014.
- [8] Bernhard Gleich and Jürgen Weizenecker. Tomographic imaging using the nonlinear response of magnetic particles. *Nature*, 435(7046):1214–1217, 2005.
- [9] Patrick W Goodwill, Justin J Konkle, Bo Zheng, Emine U Saritas, and Steven M Conolly. Projection x-space magnetic particle imaging. *IEEE transactions on medical imaging*, 31(5):1076–1085, 2012.
- [10] Michael Grant and Stephen Boyd. Graph implementations for nonsmooth convex programs. In V. Blondel, S. Boyd, and H. Kimura, editors, *Recent Advances in Learning and Control*, Lecture Notes in Control and Information Sciences, pages 95–110. Springer-Verlag Limited, 2008. [http://stanford.edu/~boyd/graph\\_dcp.html](http://stanford.edu/~boyd/graph_dcp.html).
- [11] Michael Grant and Stephen Boyd. CVX: Matlab software for disciplined convex programming, version 2.1. <http://cvxr.com/cvx>, March 2014.
- [12] Serhat Ilbey, Can Barış Top, Alper Güngör, Tolga Çukur, Emine Ülkü Saritaş, and H Emre Güven. Comparison of system-matrix-based and projection-based reconstructions for field free line magnetic particle imaging. *International Journal on Magnetic Particle Imaging*, 3(1):1–8, 2017.
- [13] Barbara Kaltenbacher, Tram Thi Ngoc Nguyen, Anne Wald, and Thomas Schuster. Parameter identification for the Landau–Lifshitz–Gilbert equation in magnetic particle imaging. In *Time-dependent Problems in Imaging and Parameter Identification*, pages 377–412. Springer, 2021.
- [14] Tobias Kluth. Mathematical models for magnetic particle imaging. *Inverse Problems*, 34(8):083001, 2018.
- [15] Tobias Kluth, Bangti Jin, and Guanglian Li. On the degree of ill-posedness of multi-dimensional magnetic particle imaging. *Inverse Problems*, 34(9):095006, 2018.
- [16] Tobias Kluth, Patryk Szwargulski, and Tobias Knopp. Towards accurate modeling of the multidimensional magnetic particle imaging physics. *New journal of physics*, 21(10):103032, 2019.
- [17] Tobias Knopp and Thorsten M Buzug. *Magnetic particle imaging: an introduction to imaging principles and scanner instrumentation*. Springer Science & Business Media, 2012.
- [18] Tobias Knopp, Marlitt Erbe, Timo F Sattel, Sven Biederer, and Thorsten M Buzug. A Fourier slice theorem for magnetic particle imaging using a field-free line. *Inverse Problems*, 27(9):095004, 2011.

- [19] Tobias Knopp, Nadine Gdaniec, and Martin Möddel. Magnetic particle imaging: from proof of principle to preclinical applications. *Physics in Medicine & Biology*, 62(14):R124, 2017.
- [20] Eli Mattingly, Erica Mason, Konstantin Herb, Monika Śliwiak, Katrin Brandt, Clarissa Cooley, and Lawrence Wald. OS-MPI: an open-source magnetic particle imaging project. *International Journal on Magnetic Particle Imaging*, 6(2 Suppl 1), 2020.
- [21] APS Mosek. The MOSEK optimization software. *Online at <http://www.mosek.com>*, 54(2-1):5, 2010.
- [22] Frank Natterer. *The Mathematics of Computerized Tomography*. 1986.
- [23] Martin Storath, Christina Brandt, Martin Hofmann, Tobias Knopp, Johannes Salamon, Alexander Weber, and Andreas Weinmann. Edge preserving and noise reducing reconstruction for magnetic particle imaging. *IEEE transactions on medical imaging*, 36(1):74–85, 2016.
- [24] Robert Tovey, Martin Benning, Christoph Brune, Marinus J Lagerwerf, Sean M Collins, Rowan K Leary, Paul A Midgley, and Carola-Bibiane Schönlieb. Directional sinogram inpainting for limited angle tomography. *Inverse Problems*, 35(2):024004, 2019.
- [25] Patrick Vogel, Jonathan Markert, Martin A Rückert, Stefan Herz, Benedikt Keßler, Kilian Dremel, Daniel Althoff, Matthias Weber, Thorsten M Buzug, Thorsten A Bley, et al. Magnetic particle imaging meets computed tomography: First simultaneous imaging. *Scientific reports*, 9(1):1–9, 2019.
- [26] Jürgen Weizenecker. The Fokker–Planck equation for coupled brown–néel-rotation. *Physics in Medicine & Biology*, 63(3):035004, 2018.
- [27] Jürgen Weizenecker, Bernhard Gleich, and Jörn Borgert. Magnetic particle imaging using a field free line. *Journal of Physics D: Applied Physics*, 41(10):105009, 2008.
- [28] Lena Zdun and Christina Brandt. Fast MPI reconstruction with non-smooth priors by stochastic optimization and data-driven splitting. *Physics in Medicine & Biology*, 66(17):175004, 2021.





(a) Reconstruction with respect to  $\mathcal{M}_2$ . ( $\alpha_1 = 4 \cdot 10^4$ ,  $\alpha_2 = 0.1^{3.75}$ ,  $\text{SSIM}(\mathbf{c}) = 0.9014$ )



(b) Reconstruction with respect to  $\mathcal{M}_3$ . ( $\alpha_1 = 1 \cdot 10^4$ ,  $\alpha_2 = 0.1^{4.7}$ ,  $\text{SSIM}(\mathbf{c}) = 0.9302$ )



(c) Reconstruction with respect to  $\mathcal{M}_2$  and noisy data. ( $\alpha_1 = 4 \cdot 10^4$ ,  $\alpha_2 = 0.1^{3.8}$ ,  $\text{SSIM}(\mathbf{c}) = 0.8689$ )



(d) Reconstruction with respect to  $\mathcal{M}_3$  and noisy data. ( $\alpha_1 = 4 \cdot 10^4$ ,  $\alpha_2 = 0.1^{3.9}$ ,  $\text{SSIM}(\mathbf{c}) = 0.8826$ )

Figure 8: Results for simultaneous line rotation using different reconstruction approaches.